Assessment of hessian-based Frangi vesselness filter in optoacoustic imaging

Antonia Longo[a,b,c], Stefan Morscher[c], Jaber Malekzadeh Najafababdi[a,b], Dominik Jüstel[a,b], Christian Zakian[a,b], Vasilis Ntziachristos[a,b,*]

[a] *Chair of Biological Imaging and TranslaTUM, Technical University of Munich, Ismaninger Str. 22, 81675, München, Germany*
[b] *Institute of Biological and Medical Imaging (IBMI), Helmholtz Zentrum München, Ingolstädter Landstr. 1, D-85764, Neuherberg, Germany*
[c] *iThera Medical GmbH, Zielstattstrasse, 13, 81379, München, Germany*

A B S T R A C T

The Hessian-based Frangi vesselness filter is commonly used to enhance vasculature in optoacoustic (photoacoustic) images, but its accuracy and limitations have never been rigorously assessed. Here we validate the ability of the filter to enhance vessel-like structures in phantoms, and we introduce an experimental approach that uses measurements before and after the administration of gold nanorods (AuNRs) to examine filter performance *in vivo*. We evaluate the influence of contrast, filter scales, angular tomographic coverage, out-of-plane signals and light fluence on image quality, and gain insight into the performance of the filter. We observe the generation of artifactual structures that can be misinterpreted as vessels and provide recommendations to ensure appropriate use of Frangi and other vesselness filters and avoid misinterpretation of post-processed optoacoustic images.

1. Introduction

Optoacoustic images typically employ the Hessian-based Frangi vesselness (HFV) filter [1] for enhancing the visualization of vasculature [2–9]. The filter is applied at an image voxel level and is based on the eigenvalue decomposition of the local Hessian matrix of the image. Thereby, the local structure of a voxel (*i.e.* tubular, blob-like or plate-like) at each scale is encoded in the sign and amplitude of the Hessian eigenvalues. By selecting specific eigenvalues and defining a vesselness function, the contrast of vessels is enhanced, while non-vascular structures and background noise are suppressed.

Several other methods have been proposed for 2D and 3D enhancement of vasculature in medical imaging based on pixel intensity, feature modelling, geometric tracking, artificial intelligence or multiscale/multiorientation algorithms [10,11]. Vessel enhancement techniques based on pixel intensity, such as skeleton-based, ridge-based and region growing-based approaches, are not suitable for OA images because signal intensity varies with depth due to light [12] and sound attenuation [13]. Moreover, at a given depth, OA signal intensities depend on the OA source dimensions (*e.g.* vessel size). Methods based on feature modelling, tracking, and artificial intelligence are mainly used for vessel segmentation rather than for contrast enhancement, as required in OA imaging. These approaches are also computationally complex and require *a priori* information to guide the segmentation

process [11]. Multiscale/multiorientation algorithms such as matching filters [14], Laplacian pyramid [15], wavelet transform [16,17], and Gabor filter [18,19] are suitable for OA, but require prior selection of anisotropic kernels and definition of a classification function for segmentation.

Instead, the Hessian-based Frangi filter is conventionally used for OA image enhancement because it employs a well-defined kernel and vessel classification function, which simplifies its implementation [1]. In OA mesoscopy and microscopy, the HFV filter has been widely employed for vasculature enhancement [20–22,5,23] and quantification [24,25]. Furthermore, hybrid enhancement techniques, such as the combination of a Gabor filter and either a standard [26] or modified Frangi vesselness filter [9,27] have been also employed to improve background noise suppression and small vessel contrast. In OA macroscopy, the HFV filter has been applied in clinical and pre-clinical studies on either fully reconstructed images [3,7,8] or separately on both positive and negative components of the reconstructed image [2].

However, the wide use of HFV filters in OA imaging necessitates a careful analysis of the influence of this enhancement algorithm on image accuracy. This is especially apparent in macroscopy where images are more susceptible to background tissue absorption and vessels suffer from reduced contrast, leading to artifacts. Indeed, simple experimentation with the HFV filter reveals that different filter parameters (scales) produce markedly different images (Fig. 1 (a)-(f)). This

finding introduces an inherent uncertainty as to which image is the most reliable representation of the object. Assuming that only one of the images generated after HFV processing is an accurate representation, other images with different filter scales then contain inaccuracies; in particular, the generation of artifactual vessels is possible. Despite this, the performance of HFV filters and the conditions under which artefacts are generated have yet to be systematically assessed.

In this work, we investigated the degree to which the HFV filter could accurately enhance vessel-like structures in optoacoustic (photoacoustic) images of two model systems: agar phantoms and a section of a mouse abdomen. We were particularly interested in identifying whether the filter improves an image quality at the expense of accuracy.

Using experimental measurements on phantoms, we systematically evaluated the contribution of HFV filter parameters to the appearance of artifacts in the images. Furthermore, we studied the accuracies of HFV-filtered images as a function of sample/tissue type, optoacoustic set-up employed, motion and other experimental parameters. Informed by our experimental results on the effects of these parameters, we then provide recommendations for the use of the HFV filter.

To assess the biological accuracy, we introduce herein a novel method for *in vivo* validation of the HFV filter in optoacoustic imaging using gold nanorods (AuNRs) as contrast agents [28,29] to label vessels in mice. We discuss the implications of using the HFV filter to improve real vessel detection in relation to preserving image features *in vivo*.

2. Methods

Optoacoustic measurements were conducted using a commercially available, real-time, multispectral optoacoustic tomographic (MSOT) small animal scanner (inVision 256-TF, iThera Medical, Munich, Germany). The acquired data were filtered using a digital band-pass filter between 300 kHz and 8 MHz and reconstructed using a conventional backprojection algorithm.

Assuming a uniform speed of sound. Then the HFV filter was applied to the 2D reconstructed images during post-processing. We proposed an optoacoustic image contrast index, CI, to quantify the OA image quality and provide an indicator for the use of HFV filter. The CI for all the reconstructed OA images was defined as the standard deviation of the absolute value of the image pixel values which are above an instrument-specific threshold; likewise calculated as the standard deviation of the absolute value of the pixels outside the imaging field of view (*i.e.* background).

To adjust image contrast, a histogram-based thresholding method was applied to all OA and HFV filtered images by removing 0.5 % highest and 0.02 % lowest pixel values. Note that the process was applied only to improve image visualization, and all quantification metrics were estimated on the raw images.

2.1. HFV filter in OA imaging

The HFV filter extracts tubular structures from an OA image by classifying the eigenvalues of the Hessian matrix *via* a vesselness function. A two-dimensional OA reconstructed image $I(\bar{x})$ is observed at a scale $s > 0$ by convolution with a Gaussian kernel $G_s(\bar{x})$ with standard deviation s. The normalized Hessian matrix $H(\bar{x}, s)$ of the resulting image $I_s(\bar{x}) = I * G_s(\bar{x})$ at scale s is then given by:

$$H(\bar{x}, s) = B \frac{\partial^2}{\partial \bar{x}^2} I_s(\bar{x}) = B\left(\frac{\partial^2}{\partial \bar{x}^2} G_s \right) * I(\bar{x}),$$

(1)

Where B is a normalization factor, and the second equality follows by partial integration and is used for implementation. The 2D Frangi vesselness function for vessels with bright contrast (as in OA) is defined as:

$$v(\bar{x}, s) = \begin{cases} 0 \text{ if } \lambda_2(\bar{x}, s) > 0 \\ exp\left(-\frac{R_b^2(\bar{x}, s)}{2\beta_1^2} \right)\left(1 - exp\left(-\frac{S^2(\bar{x}, s)}{2\beta_2^2} \right) \right) \end{cases}$$

(2)

Where $\lambda_1(\bar{x}, s)$ and $\lambda_2(\bar{x}, s)$ are the sorted eigenvalues $(|\lambda_1(\bar{x}, s)| < |\lambda_2(\bar{x}, s)|)$ of the image Hessian at position $\bar{x}$ at scale s; $R_b^2(\bar{x}, s) = \frac{|\lambda_1(\bar{x}, s)|}{|\lambda_2(\bar{x}, s)|}$ and $S^2(\bar{x}, s) = \sqrt{\lambda_1(\bar{x}, s) + \lambda_2(\bar{x}, s)}$ are the *blobness* and *structureness* measures [1], respectively used to distinguish vessels from blob-like structures and noise/background; parameters β_1 and β_2 tune the sensitivity of the filter to the measures R_b and S.

The values of β_1 and β_2 are set heuristically to suppress blob-like structure and background noise (*i. e.* $\beta_1 = 1$; $\beta_2 = \frac{\max_{\bar{x}} S^2(\bar{x}, s)}{2}$), in agreement with Refs. [1,30], and [4]. The range of scales s are selected to enhance vessels from one half to six times the system resolution of 165 μm (*i.e.* scaled between 2 and 10 pixels). The final vessel-enhanced image is obtained by analyzing the vesselness function in Eq. (2) at different scales s and by blending (summing) the filter responses.

2.2. Phantom measurements

Phantom measurements were first performed to investigate the effect of image contrast, filter scales, light fluence, limited tomographic angular coverage, out-of-plane signal, proximity to air cavities. Five phantoms were produced with different optical properties. Optoacoustic signals of different intensities were obtained by printing black or grey vessel-like shapes on white paper, then embedding them in turbid agar cylinders (12-mm diameter) made with 3% (w/v) agar (Fluka Analytical, Germany) and 6% (v/v) intralipid (20 % stock solution; Sigma Aldrich, Germany). All the phantoms show similar scattering properties as tissues (~ 10 cm^{-1}); in two of them, India ink (Higgins Ink, Leeds, MA, USA) was added to simulate background absorption, resulting in an absorption of 0.05 OD.

Note that the addition of paper into agarose phantom could lead to water ingress into the paper, which could result in a degradation of the reference structure. However, this remains a common factor on all tests presented.

After preparation, all the phantoms were positioned in the center of the MSOT chamber and imaged at a water temperature of 34 ˚C. The HVF filter was then applied on all the optoacoustic reconstructed images with scales ranging between 2 and 10 pixels. Other filter parameters were tuned to classify vessels while reducing the enhancement of blob-like structures and noise, and in agreement with Bouattour and Paulus [30].

All unfiltered optoacoustic images and corresponding HFV-filtered images were qualitatively compared using the structural similarity index (SSIM) previously reported by Wang et al. [31].

2.3. In vivo measurements

In vivo measurements were conducted to validate the HFV filter by imaging mouse injected with commercially available AuNRs with an absorption peak of 780 nm (Ntracker D12M-10−780-50, Nanopartz, Loveland, CO, USA). These AuNRs serve as an exogenous contrast agent to label vessels [28,29]. Animal procedures were approved by the Government of Upper Bavaria. A nude mouse (4 weeks old, 18.7 g) was anesthetized and a catheter inserted into its tail vein for AuNR injection. The mouse was placed lying prone in the animal holder such that the transducer array faced the ventral side. A section through the abdomen was chosen as the anatomical region of interest for optoacoustic imaging. The two kidneys were selected to demonstrate the broadband capability of the technology in an organ with well-defined features of varying scales. 40 μL of 78 nM AuNRs were injected intravenously in the animal, an amount that our pilot studies indicated can provide high optical contrast while preventing fluence attenuation effects in the
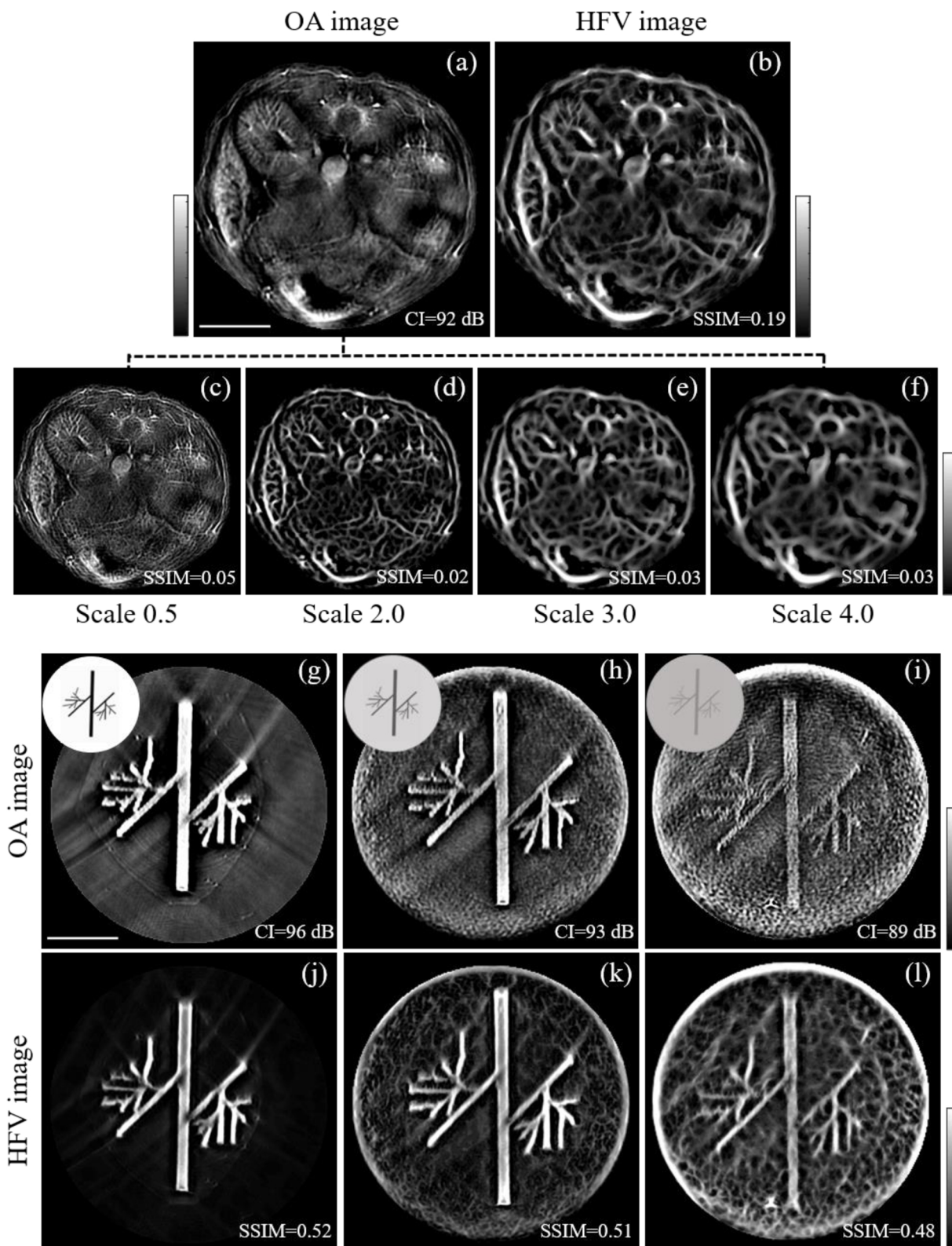
Fig. 1. Effect of different optoacoustic contrast and filter scales on the performance of the HFV filter. The *top panel* shows the reconstructed optoacoustic image of a mouse abdomen section **(a)** and HFV filtered image for scales 0.5 **(c)**, 2.0 **(d)**, 3.0 **(e)** and 4.0 **(f)**, respectively, to enhance vessel diameters ranging from one half to six times the system resolution of 165 um. Resulting multi-scale blend (average) of the HFV filtered images of the mouse abdomen **(b)**. The *bottom panel* shows the experimental validation of the HFV filter application to optoacoustic phantom images with different optoacoustic contrast CI **(g, h, i)** and corresponding HFV filtered images **(j, k, l)**. The insets at the upper left of panels (g), (h) and (i) show the vessel-like printed papers used to simulate different optoacoustic absorption (black and grey) and the corresponding absorbing agar phantoms. HFV: Hessian-based Frangi vesselness, SSIM: structure similarity index, CI: contrast index.

mouse abdomen (data not shown). Optoacoustic data were continuously acquired at 780 nm for 3 min before AuNRs injection, during the 15 s of the injection, and for 6 min after injection. This resulted in a total of 5400 frames (10 frames-per-second, limited by the laser repetition rate of 10 Hz). After data acquisition, the mouse was euthanized by cervical dislocation. Prior to applying the HFV filter *in vivo*, a post-processing breath-gating strategy was applied to all reconstructed images in order to reduce motion artifacts due to respiration, as well as signal amplitude variations due to changes in blood oxygenation during breathing. Pre- and post-injection images were accurately aligned as follows. First, we observed an OA signal amplitude variation in time among all the frames with a periodicity of 1 Hz due to respiratory frequency of the mouse. Second, we extracted the expiratory frames (from inhalation, respiratory peak and exhalation frames) before and after injection by windowing the signal and selecting only the time points where the OA signal amplitude has a local maximum. Then, we averaged the extracted frames at the expiratory pauses to increase SNR. Finally, the alignment accuracy between averaged frames before and after injection was quantified using the SSIM index.

3. Results

Using optoacoustic images of phantoms, we independently assessed the impact of different HFV filter parameters on contrast, tomographic angular coverage, out-of-plane signal, acoustic reflections and light fluence.

Since the signal-to-noise ratio (SNR) in tomographic optoacoustic images may vary depending on depth and other experimental parameters, we first tested the performance of the filter under different optoacoustic contrast conditions. For this purpose, three OA phantoms with different optoacoustic contrast index CI were produced by changing the absorption of the agar and the printed phantom. Fig. 1 (g) and (j) show the unfiltered optoacoustic image and corresponding HFV filtered image for the phantom with the highest CI of 96 dB. This phantom was obtained by embedding black printed vessel-like shape in agar without background absorption. By adding background absorption in steps of 0.05 optical density and changing the absorbing phantom from black to grey, we also obtained images at CI of 93 dB (Fig. 1 (h) and (k)) and CI of 89 dB (Fig. 1 (i) and (l)). The images clearly show that application of the HFV filter results in the appearance of artifactual blood vessels. For example, Fig. 1 (l) shows that the appearance of the printed structure improves. Nevertheless, we also observe the appearance of a multitude of interconnected small vessels throughout the image.

Though these "vessels" appear realistic, they are present in areas of the object where only white paper exists. A similar effect is also observed in Fig. 1 (l). The generation of artificial vessel structures from background absorption results in a reduced structure similarity index (SSIM) value as the CI decreases.

To study whether such performance persists in animal imaging, we considered an optoacoustic cross-sectional image from a mouse abdomen obtained *in-vivo*. Fig. 1 (a) shows the unprocessed image of the abdomen, showing the kidneys, spinal cord and spleen of the mouse, among other morphological features. Fig. 1 (c)-(f) show HFV processing of Fig. 1 (a) with a different scale. As observed, increasing the scale leads to the appearance of an elaborate network of vessels with ever-greater diameters that do not exist in the original image. Finally, Fig. 1 (b) shows a composite image that was obtained by blending (adding) the images in Fig. 1 (c)-(f) to one image. The results shown in Fig. 1 demonstrate that application of the HFV filter can lead to artifactual images that overestimate vascular networks in optoacoustic images, compromising fidelity and accuracy. For instance, noise and random morphological features in the original image may be transformed into vessel-like structures. Indeed, comparing the HFV filtered images at each scale in Fig. 1(c)-(f) clearly demonstrates biological inconsistency among the enhanced features.

Having established that the CI of an image can affect HFV filter performance and lead to the generation of artifacts, we examined whether this unreliability was even stronger in the more realistic situation of limited-view coverage. For practical reasons, all commercial optoacoustic tomography systems collect data from less than 360 degrees around the sample, meaning that artifacts generated by the reconstruction algorithms [32] remain in the post-processed HFV filtered images. Limited tomographic views were tested by reducing the number of reconstructed channels for the phantom with highest CI from 270° [original, Fig. 1 (g)] to 125° [Fig. 2 (a)], that is usually the angular coverage of the clinical handheld optoacoustic systems. As seen in Fig. 2 (b) the filter highlights the ray artifacts that resulted from the limited view acquisition and reconstruction shown in Fig. 2 (a). Thus, HFV filter must be applied with care when full angular coverage in not guaranteed.

A further analysis was then carried out to examine how air cavities near the image plane affect filter performance. In optoacoustic tomography, especially for small animal systems, organs of interest in the abdomen sections (*e.g.* liver or kidneys) are in the same field of view as certain air-containing regions (*e.g.* lungs, stomach or intestines). No optoacoustic signal is expected from these regions and additional acoustic reflections may be generated due to acoustic mismatch. To
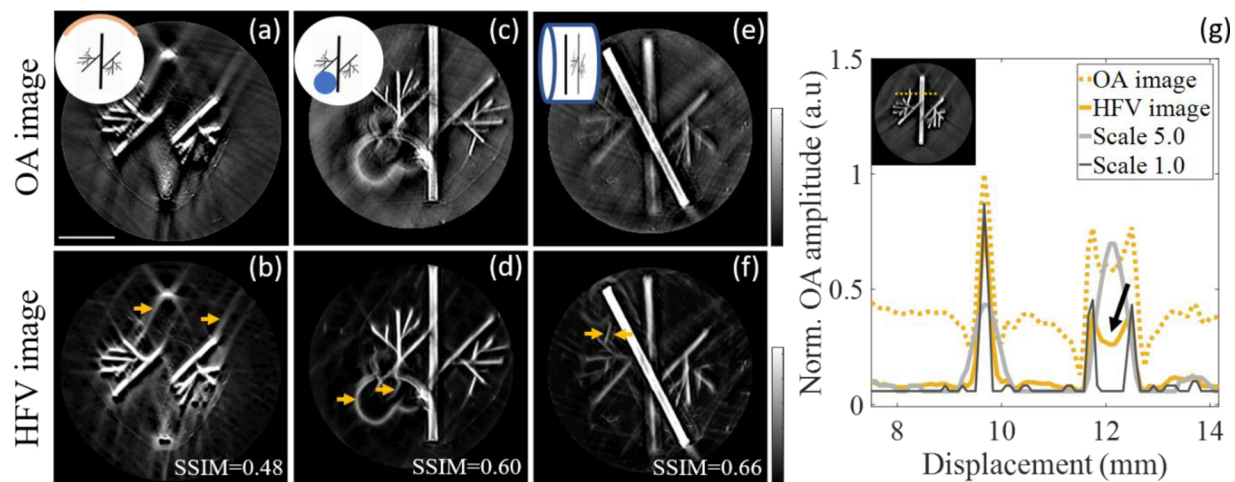

Fig. 2. Effect of different system characteristics on the performance of the HFV filter in experimental optoacoustic phantoms. Limited tomographic view **(a, b)**, presence of an air cavity **(c, d)**, out-of-plane signal **(e, f)**, different filter scales and contrast variation in a large vessel **(g)**. Arrows show artifacts enhancement after HFV filter.

simulate such cavities, a tubular hole of 3 mm diameter was introduced along the agar cylinder containing the vessel-like printed phantom. Enhanced artifacts can be seen in the HFV filtered image in Fig. 2 (d), which are a result of strong ultrasound reflections at the air cavity boundary; artifactual vessels appear in the cavity where no OA signal is expected.

We also questioned the influence of out-of-plane signals on the HFV filter performance. Although cylindrically focused transducers are usually employed in tomographic systems to minimize sensitivity to signals outside the image plane [33,34], they still detect low-frequency signals from other planes due to the diffuse illumination. To simulate such an effect, a black transversal line was printed on white paper and positioned at the image plane, while the out-of-plane signal was produced by placing the grey vessel-like printed phantom 700 nm away from the image plane. No out-of-plane effects were observed for separations above 1 mm from the image plane (data not shown), which corresponds to the elevation resolution of the transducer array. Fig. 2 (e) and (f) show the low-frequency content of the out-of-plane signal from the vessel-like printed shape and the HFV filtered image. As shown in the figure, structures out of the image plane and not in focus can be falsely enhanced, and appear as double structures.

Finally, we investigated the effect of different filter scales on image resolution, since these scales are usually tuned empirically according to system resolution and image quality. Fig. 2 (g) shows the intensity line profiles of the unfiltered and corresponding HFV-filtered optoacoustic images of the phantom with the highest CI, and the effect of small scale (Scale 1.0) or large scale (Scale 5.0). The figure shows that while the large scales compromise the resolution of small structures, the small scales enhance only structural edges. Moreover, a depth-dependent contrast variation in a large vessel due to light fluence [arrow in Fig. 2 (g)] can be intensified by the filter using small scales. These examples demonstrate that, although filter scales are carefully chosen, the

response of the filter is typically not uniform between vessels of different radii.

After assessing the performance of the filter under different conditions, we rigorously validated our findings *in vivo*. In particular, we examined the ability of the HFV filter to improve real vessel detection while preserving image features. For this purpose, we injected gold nanorods (AuNRs) into a nude mouse to act as exogenous contrast agents to label vessels. We then used the differential optoacoustic image, obtained by subtracting the image pre-injection from the image post-injection, as the gold standard for vessel localization for comparison with the HFV-filtered image.

Prior to validation, we implemented a post-processing breath-gating strategy to assure proper co-registration between the images pre- and post-injection, as well as to avoid misalignment artefacts in the differential image. Fig. 3 (a)-(d) show the optoacoustic images of the mouse abdomen section at different breathing points during a single respiratory cycle captured over 12 consecutive frames. The respiration frequency was maintained at 60–70 bpm [35]. Motion artifacts were quantified using the SSIM index, with the optoacoustic reconstructed image at the expiratory pause taken as a reference, which was then compared with the optoacoustic images at three successive breathing points: inhalation (Fig. 3 (b)), respiratory peak (Fig. 3 (c)), and exhalation (Fig. 3 (d)). The optoacoustic images at the different breathing points show diverse anatomical features due to motion. The arrows in the images highlight the differences in the left and right kidney in a single respiratory cycle. The misalignment between the respiratory frame and the other frames was also confirmed by the low SSIM indices, ranging from 0.61 to 0.75.

Having assessed the effect of breathing motion, the respiratory artefacts were corrected by tracking the optoacoustic signal amplitude variation in the mouse abdomen, as shown in Fig. 3 (e). As observed from the graph, the optoacoustic signal variation shows a periodicity of
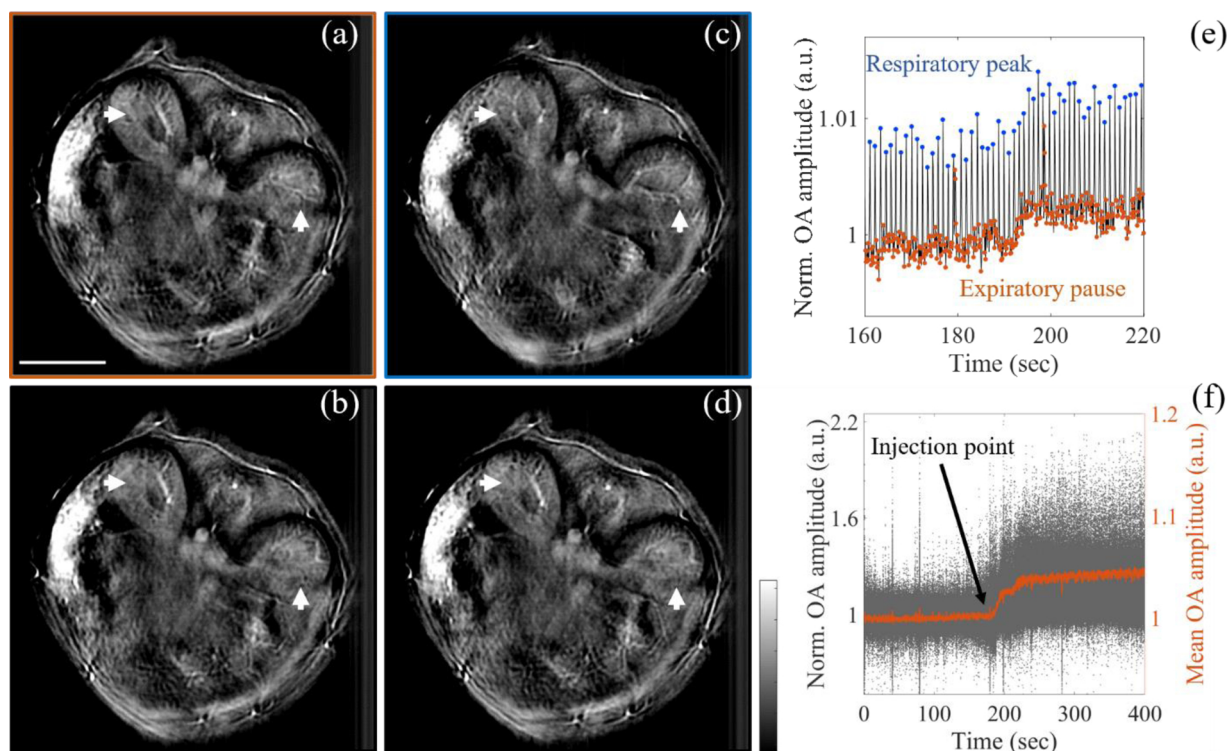
Fig. 3. Breathing correction and kinetics of AuNRs perfusion *in vivo*. (a-d) optoacoustic images of mouse abdomen showing the left and right kidneys (arrows) at four different breathing points: **(a)** expiratory pause, **(b)** inhalation, **(c)** respiratory peak and **(d)** exhalation. The SSIM was used here as a metric to quantify the breathing motion between the expiratory frame (reference) and the other frames. **(e)** Normalized optoacoustic signal in the mouse abdomen across the injection time point showing breathing motion artifacts. Animals were injected with AuNRs over the indicated interval in order to enhance vessels. **(f)** Visualization of the AuNR perfusion in the selected expiratory frames after breathing correction.
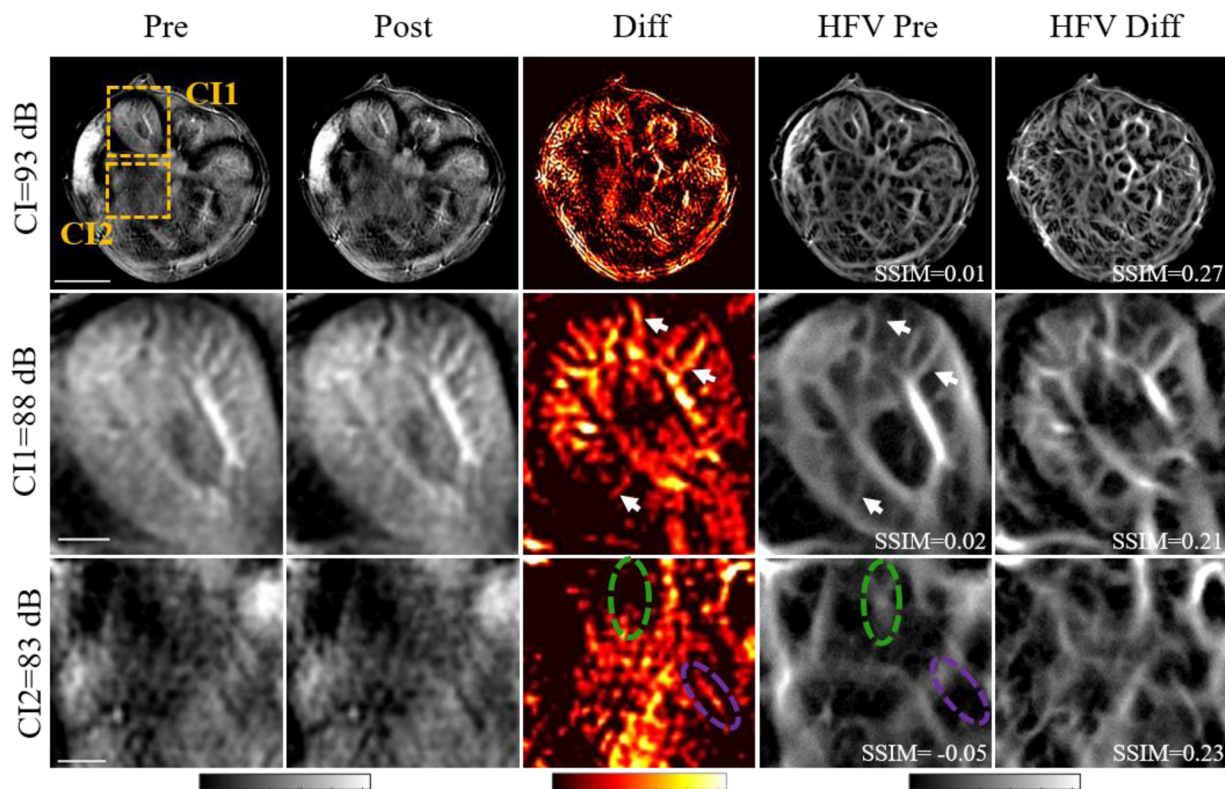
Fig. 4. *In vivo* **validation of the HFV filter shows enhancement of real and false vessels in mouse abdomen at 780 nm.** *Top row:* unfiltered optoacoustic images of the mouse abdomen. The boxes indicate regions of interest also analysed as zoomed-in views. Vessel-enhanced images (Diff), generated as described in the text, were compared with the optimized HFV filtered pre-injection image (HFV Pre) and HFV-filtered difference image (HFV Diff) in terms of the structure similarity index (SSIM). *Middle row:* Zoomed-in view of a region of interest in the left kidney with CI 88 dB. Enhancement of real vessels after HFV filter are marked with white arrows. *Bottom rows:* Zoomed-in view of a region closer to the stomach with CI 83 dB. Due to low OA contrast, HFV filter creates false vessel-like structures from the background (green circle) or fails to enhance true vessels (purple circle).

the respiratory frequency (~60–70 bpm), with the maximum values at the respiratory peaks and minimum values during the expiratory pauses. Therefore, only the frames corresponding to the expiratory pause were selected for breathing motion correction.

The results in Fig. 3 (f) show the kinetics of AuNRs perfusion in those selected frames. The graph reported a first increase of the optoacoustic signal after AuNRs injection (~15 s, injection duration), followed by a first plateau and a second increase up to a maximum value. After injection, the mean optoacoustic signal increased by 5% while the highest improvement of the optoacoustic amplitude was of 100 %.

Finally, the resulting frames were averaged to have single co-registered frames at pre- and post-injection periods (Pre and Post images in Fig. 4, *top row*), resulting in an alignment score of 0.95 (SSIM). optoacoustic images aligned in this manner were analyzed to validate the HFV filter *in vivo*.

Fig. 4 shows the *in vivo* validation of the HFV filter. The positive difference images (Diff) were calculated by subtracting the pre-injection image from the aligned post-injection image. The difference images were then compared with the optimized HFV filtered pre-injection images (HFV Pre) using SSIM. The optimized HFV filter was also applied to the Diff image (HFV Diff) for comparison, and the SSIM between HFV Diff and Diff image was calculated to quantify the highest similarity for the case the HFV filter is applied to the vessel-enhanced images (difference images).

Two regions of interest (ROIs) within the abdomen section were selected and magnified for further analysis: a region in the right kidney with higher CI (88 dB), and a region closer to the stomach with a lower CI (83 dB). The *in vivo* validation results show an overall visual improvement in the optoacoustic contrast after HFV filtering at the

expense of biological accuracy in regions with low optoacoustic contrast. In the highly vascularized regions, *e.g.* the right kidney region (CI = 89 dB), vessels are enhanced after filtering (white arrows in the figure); in the region close to the stomach with a lower CI (CI = 83 dB), false vessel-like structures are created from the background (green circle in the figure) or true vessels are not enhanced (purple circle in the figure), leading to a negative SSIM index (-0.05). Indeed, the comparison between the HFV Pre image and HFV Diff image highlights the importance of adequate CI for accurate representation of vessel structure using HFV filter.

4. Discussion and conclusion

In this work, we examined whether application of the common HFV filter, used to enhance vessel contrast, compromises optoacoustic image fidelity. The study included both controlled phantom measurements and animal images obtained under different experimental conditions. We demonstrated that the performance of the filter varies with the CNR and morphological features of the image, and that this variation can result in the appearance of distorted or non-existent vasculature. Notably, we observed both *in vivo* (Fig. 1 (a)-(f)) and in phantoms (Fig. 1 (g) and (l)) that the filter generates false vessel-like structures from random patterns of background tissue absorption in optoacoustic tomographic images. In addition, when the HFV filter was applied at different scales on an *in vivo* OA image (Fig. 1 (c)-(f)), vessel sizes were distorted, leading to low SSIM indices. These findings call into the question at which conditions the HFV filter can be accurately applied in *in vivo* optoacoustic imaging. Therefore, a critical assessment is required as to whether improvements in the visual appearance of an image come at the expense of image accuracy.

The combination of both, the parameters of the filter and the properties of the sample, influence the performance of the HFV filter. In order to isolate these effects, we applied the HFV filter to optoacoustic images of phantom models, as well as biological tissue (cross-section of a mouse abdomen). Specifically, we isolated the effects of the filter scale, CI of the image, detector coverage, vessel size and the presence of air, and attempted to understand qualitatively the contribution of each to the accuracy of the final image. The choice of filter scale presents a trade-off; a large scale may blur small structures, while a small scale may lead to the enhancement of edges. Thus, the filter is more successful when applied to vessels that are relatively homogeneous in size. It is also clear from our results that artifacts caused by limited detector view and air are enhanced by the HFV filter (Fig. 2 (a)-(f)), stressing the need for appropriate angular coverage and the avoidance of air cavities. Lastly, we confirmed that the intensification of artifacts is more pronounced as the CI of the image decreases. Therefore, since the contrast-to-noise ratio of optoacoustic images vary with depth, these findings imply that the performance of the HFV filter is also depth-dependent, and that artifactual vessels can be generated in deeper fields of view.

We systematically validated the performance of the HFV filter *in vivo* by comparing filtered optoacoustic images of a mouse abdomen to unfiltered images of the same region after enhancement of the real vessels with injected gold nanorods. When compared to the nanorod-labelled vessels, it was clear that the vasculature network was not faithfully reproduced in the HFV-filtered images (Fig. 4). We observed that false vessel-like structures were created from bulky tissue signal while true vessels were not enhanced. Furthermore, this *in vivo* experiment confirmed our *ex vivo* observations that the HFV filter behaves unreliably in regions of interest with low CI, such as close to the stomach or intestines, or in regions containing only pure background tissue absorption.

Overall, while application of the HFV filter offers an apparent improvement of the visual appearance of the image, populating the image space with vessels and reducing noise, we demonstrate here that this application may be problematic as it produces inconsistent and possibly misleading results when applied to currently available optoacoustic images obtained under realistic conditions. Specifically, the filter does not cope well with variations in depth and contrast index and it is susceptible to errors associated with a limited-view detection, or when air pockets are present in the subject. We found that the most reliable application of the filter was done on (1) images with a CI of 96 dB or more, (2) images obtained with transducer angular coverage higher than 270°, (3) images with no evident artifacts from air cavities in the image plane and (4) images whereby contrast and signal are corrected for depth dependency. We believe that future efforts should focus on improving the fundamentals of optoacoustic image quality and minimize the need for the application of the HFV filter, for example by increasing *in-vivo* CI values and employing signal processing approaches, such as frequency decomposition analysis.

Declaration of Competing Interest

The authors declare that there are no conflicts of interest.

Acknowledgements

References

[1] R.F. Frangi, W.J. Niessen, K. Vincken, M.A. Viergever, Multiscale vessel enhancement filtering, International Conference on Medical Image Computing and Computer-Assisted Intervention – MICCAI 1998, Springer, 1998, pp. 130–137.

[2] L. Li, L. Zhu, C. Ma, L. Lin, J. Yao, L. Wang, K. Maslov, R. Zhang, W. Chen, J. Shi, L.V. Wang, Single-impulse panoramic photoacoustic computed tomography of small-animal whole-body dynamics at high spatiotemporal resolution, Nat. Biomed. Eng. 1 (0071) (2017).

[3] L. Lin, P. Hu, J. Shi, C.M. Appleton, K. Maslov, L. Li, R. Zhang, L.V. Wang, Single-breath-hold photoacoustic computed tomography of the breast, Nat. Commun. 9 (2352) (2018).

[4] T. Oruganti, J. Laufer, B.E. Treeby, Vessel filtering of photoacoustic images., 2013, Proceedings of SPIE 8581, Photons Plus Ultrasound: Imaging and Sensing (2013).

[5] D. Soliman, G. Tserevelakis, M. Omar, V. Ntziachristos, Combined label-free optical and optoacoustic imaging of model organisms at mesoscopy and microscopy resolutions, Proceedings of SPIE 9708, Photons Plus Ultrasound: Imaging and Sensing (2016).

[6] D. Wang, Y. Wang, W. Wang, D. Luo, U. Chitgupi, J. Geng, Y. Zhou, L. Wang, J.F. Lovell, J. Xia, Deep tissue photoacoustic computed tomography with a fast and compact laser system, Biomed. Opt. Express 8 (1) (2016) 112–123.

[7] L. Li, A.A. Shemetov, M. Baloban, P. Hu, L. Zhu, D.M. Shcherbakova, R. Zhang, J. Shi, J. Yao, L.V. Wang, V.V. Verkhusha, Small near-infrared photochromic protein for photoacoustic multi-contrast imaging and detection of protein interactions in vivo, Nat. Commun. 9 (2734) (2018).

[8] E. Mercep, J.L. Herraiy, X.L. Dean-Ben, D. Razansky, Transmission-reflection optoacoustic ultrasound (TROPUS) computed tomography of small animals, Light Sci. Appl. 8 (18) (2019).

[9] P. Wray, L. Lin, P. Hu, L.V. Wang, D. Paulus, Photoacoustic computed tomography of human extremitis, J. Biomed. Opt. 24 (2) (2019) 1–8.

[10] T. Jerman, F. Pernus, B. Likar, Z. Spiclin, Enhancement of vascular structures in 3D and 2D angiographic images, IEEE Trans. Med. Imaging 35 (9) (2016) 2107–2118.

[11] C. Kirbas, F.K.H. Quek, A review of vessel extraction techniques and algorithms, ACM Comput. Surv. 36 (2) (2004).

[12] S.L. Jacque, B.W. Pogue, Tutorial on diffuse light transport, J. Biomed. Opt. 13 (4) (2008).

[13] B.E. Treeby, Acoustic attenuation compensation in photoacoustic tomography using time-varian filtering, J. Biomed. Opt. 18 (3) (2013).

[14] S. Chaudhuri, S. Chatterjee, N. Katz, M. Nelson, Detection of blood vessels in retinal images using two-dimensional matched filters, IEEE Trans. Med. Imaging 8 (3) (1989) 263–269.

[15] S. Dippel, M. Stahl, R. Wiemker, T. Blaffert, Multiscale contrast enhancement for radiographies: laplacian Pyramid versus fast wavelet transform, IEEE Trans. Med. Imaging 21 (4) (2002) 342–353.

[16] A. Laine, J. Fan, W. Yang, Wavelets for contrast enhancement of digital mammography, IEEE Eng. Med. Biol. Mag. 14 (5) (1999) 536–550.

[17] M. Usman Akram, A. Atzaz, S. Farrukh Aneeque, S.A. Khan, Blood vessel enhancement and segmentation using walevet transform, 2009 International Conference on Digital Image Processing (2009).

[18] J.V.B. Soares, J.J.G. Leandro, R.M. Cesar, H.F. Jelinek, M.J. Cree, Retinal vessel segmentation using the 2-D Gabor wavelet and supervised classification, IEEE Trans. Med. Imaging 25 (9) (2006) 1214–1222.

[19] K.Q. Sun, N. Sang, Morphological enhancement of vascular angiogram with multiscale detected by Gabor filters, Electron. Lett. 44 (2) (2008) 86–87.

[20] F.H. Zhang, K. Maslov, M.L. Li, G. Stoica, L.V. Wank, In vivo volumetric imaging of subcutaneous microvasculature by photoacoustic microscopy, Optical Express 14 (20) (2006) 9317–9323.

[21] R. Bi, U.S. Dinish, C.C. Goh, T. Imai, M. Moothanchery, X. Li, J.Y. Kim, S. Jeon, Y. Pu, C. Kim, L.G. Ng, L.V. Wang, M. Olivo, In vivo label- free functional photoacoustic monitoring of ischemic reperfusion, J. Biophotonics 12 (7) (2019).

[22] P.H. Reza, K. Bell, W. Shi, J. Shapiro, R.J. Zemp, Deep non-contact photoacoustic initial pressure imaging, Optica 5 (7) (2018) 814–820.

[23] A. Orlova, M. Sirotkina, E. Smolina, V. Elagin, A. Kovalchuk, I. Turchin, P. Subochev, Raster-scan optoacoustic angiography of blood vessel development in colon cancer models, Photoacoustics 13 (2019) 25–32.

[24] Z. Yang, J. Chen, J. Yao, R. Lin, J. Meng, C. Liu, J. Yang, X. Li, L.W. Wang, S. Song, Multi parametric quantitative microvascular imaging with optical-resolution photoacoustic microscopy *in vivo*, Opt. Express 22 (2) (2014) 1500–1511.

[25] T. Liu, M. Sun, N. Feng, Z. Wu, Y. Shen, Multiscale Hessian filter-based segmentation and quantification method for photoacoustic microangiography, Chinese Opt. Lett. 13 (9) (2015) 091701.

[26] I.U. Haq, R. Nagaoka, T. Mokino, T. Tabata, Y. Saijo, 3D Gabor wavelet based vessel filtering of photoacoustic images, Annual International Conference of the IEEE Engineering in Medicine and Biology Society, IEEE Engineering in Medicine and Biology Society, 2016.

[27] H. Zhao, K. Li, N. Chen, K. Zhank, L. Wank, R. Lin, X. Gong, L. Song, Z. Liu, C. Liu, Multiscale vascular enhancement filter applied to in vivo morphological and functional photoacoustic imaging of rat ocular vasculature, IEEE Photonics J. 11 (6) (2019).

[28] W. Li, X. Chen, Gold nanoparticles for photoacoustic imaging, Nanomedicine 10 (2)

(2015) 299–320.

[29] J. Weber, P.C. Beard, S.E. Bohndiek, Contrast agents for molecular photoacoustic imaging, Nat. Methods 13 (2016) 639–650.

[30] S. Bouattour, D. Paulus, Vessel enhancement in 2D angiographic images, International Conference of Functional Imaging and Modeling of Heart – FIMH 2007 (2007) 41–49.

[31] Z. Wang, A.C. Bovik, H.R. Sheikh, E.P. Simoncelli, Image quality assessment: from error visibility to structural similarity, IEEE Trans. Image Process. 13 (4) (2004) 600–612.

[32] Y. Xu, L.V. Wang, G. Ambartsoumian, P. Kuchment, Reconstructions in limited view thermoacoustic tomography, Med. Phys. 31 (4) (2004) 724–733.

[33] A. Rosenthal, V. Ntziachristos, D. Razansky, Model-based optoacoustic inversion with arbitrary-shape detectors, Med. Phys. 38 (7) (2011) 4285–4295.

[34] W.C. Vogt, C. Jia, K.W. Wear, B.S. Garra, T.J. Pfefer, Evaluation of Out-of-plane sensitivity and artifacts in photoacoustic imaging, Frontiers in Optics 2017, (2017).

[35] J. Joseph, M.R. Tomaszewski, I. Quiros-Gonzales, J. Weber, J. Brunker, S.E. Bohndiek, Evaluation of precision in optoacoustic tomography for preclinical imaging in living subjects, J. Nucl. Med. 58 (5) (2017) 807–814.

Antonia Longo is currently a Ph.D. student in the Institute for Biological and Medical Imaging (IBMI) at Technische Universität **München** and Helmholtz Zentrum München, Germany. She received her M.Sc in Biomedical engineer from the University of Pisa, Italy. Her research interests are in biomedical imaging, signal processing and inverse problems.

Stefan Morscher completed his degree at the faculty for electrical engineering at Technische Universität München with his Master thesis on optoacoustic imaging under Prof Vasilis Ntziachristos. Thereafter, he joined the R&D team of the newly founded iThera Medical to make MSOT available to the scientific community, where he is now leading R&D efforts for software and algorithms. He maintains close ties with many researchers in the field of otoacoustics and pushes for standardization of photoacoustic imaging under IPASC.

Jaber Malekzadeh-Najafabadi, M.Sc, is a PhD student at institute of biological and medical imaging (IBMI), Technical University of Munich. He received his M.Sc in communications engineering from Sharif University of Technology, Iran. His scientific interests cover optoacoustic imaging and data analysis.

Dr. Dominik Jüstel studied mathematics and informatics at the Technical University of Munich (TUM), graduating at the Chair for Mathematical Modeling of Biological Systems in association with the Institute for Biomathematics and Biometry at the Helmholtz Center Munich. He received his doctoral degree (Dr. rer. nat.) in mathematics with highest distinction at the Chair for Analysis at TUM. After a postdoc at the mathematics faculty of TUM, Dr. Jüstel joined the Chair for Biological Imaging at TUM and the Institute for Biological and Medical Imaging at the Helmholtz Center Munich. With his group for Computation & Analytics at TranslaTUM, he works on quantitative multispectral optoacoustic tomography and advanced data analysis for various optical and optoacoustic imaging modalities.

Dr. Christian Zakian is the Group Leader for Optoacoustic Endoscopy at the Helmholtz Zentrum München. His main research interest is in the translation and adoption of optical and optoacoustic imaging methods to assist in medical diagnosis, and in particular for advanced endoscopy. He received his PhD in physics from the University of Manchester in 2007 and has complemented his background with a life sciences Masters degree in the field of Inflammation at the William Harvey Research Institute, Queen Mary University London, in 2013. He has over 15 years' experience developing diverse imaging methods implemented for clinical studies.

Professor Vasilis Ntziachristos studied Electrical Engineering at Aristotle University in Thessaloniki, Greece and received his M.Sc. and Ph.D. from the Bioengineering Department of the University of Pennsylvania. He served as assistant professor and director of the Laboratory for Bio-Optics and Molecular Imaging at Harvard University and Massachusetts General Hospital. Currently, he is the Director of the Institute for Biological and Medical Imaging at the Helmholtz Zentrum in Munich, Germany, as well as a Professor of Electrical Engineering, Professor of Medicine and Chair for Biological Imaging at the Technical University Munich, Germany. His work focuses on novel innovative optical and optoacoustic imaging modalities for studying biological processes and diseases as well as the translation of these findings into the clinic.